ANNALS OF GEOPHYSICS, 69, 1, S113, 2026; doi:10.4401/ag-9425
OPEN ACCESS

Investigating Stress Transfer and Fault Interaction in the July-August 2025 Poso and Tokararu Earthquakes, Central Sulawesi, Indonesia

Joshua Purba[*,1], Ramadhan Priadi[1], Kevin Hanyu Clinton Wulur[1], Imanuela Indah Pertiwi[2]

(1) Gowa Geophysical Station, Agency for Meteorology Climatology and Geophysics, BMKG, Gowa, Indonesia
(2) Kendari Geophysical Station, Agency for Meteorology Climatology and Geophysics, BMKG, Kendari, Indonesia

Article history: received September 12, 2025; accepted February 12, 2026

Abstract

The July-August 2025 earthquake in Central Sulawesi, which consisted of the Mw 5.9 Poso strike-slip event and the Mw 6.0 Tokararu thrust event, offers new insights into stress transfer and fault interaction in a tectonically complex setting. We combined Coulomb stress modeling, HypoDD aftershock relocation, and ascending-track DInSAR analysis to investigate the sequence. Relocation of 669 events sharpened fault geometries, with aftershocks of the Poso earthquake clustering along the Poso-West segment and those of Tokararu aligning on a shallow thrust plane. Coulomb stress modeling shows that aftershocks correlate well with positive ΔCFS lobes for both events, supporting static stress transfer as a key mechanism, though no significant positive stress was transferred from Poso to Tokararu. DInSAR results reveal both pre- and co-seismic deformation, with uplift reaching +16 cm and subsidence −13 cm at Poso, and uplift up to +13 cm and subsidence −14 cm at Tokararu. These signals suggest strain accumulation and possible aseismic slip preceding rupture. Geological contrasts within the Pompangeo Complex, where weak alluvial sediments overlie stronger metamorphic basement rocks, further explain the differences in rupture style. Together, these multidisciplinary findings highlight the interplay of tectonic loading, fault mechanics, and lithological heterogeneity in shaping cascading earthquake hazards in Central Sulawesi.

Keywords: Coulomb Stress Transfer; Earthquake Relocation; Dinsar; Fault Interaction; Central Sulawesi

1. Introduction

Central Sulawesi, Indonesia (Fig. 1), is among the most tectonically active regions in Southeast Asia, characterized by the complex interaction of multiple fault systems, including the Palu-Koro, Matano, Poso, and Tokararu Faults (Irsyam et al., 2020; Natawidjaja et al., 2021; Hanif et al., 2024; Serhalawan and Chen, 2024; Trismahargyono et al., 2024). The intricate seismotectonic framework of this region makes it highly susceptible to destructive earthquakes, as demonstrated by the 2018 Mw 7.5 Palu earthquake and subsequent seismic crises (Frando et al., 2025;

Natawidjaja et al., 2021; Supendi et al., 2019). Compared to the extensively studied Palu-Koro Fault (Frando et al., 2025; Natawidjaja et al., 2021; Supendi et al., 2019), the Poso and Tokararu Faults remain relatively understudied, despite their proximity to populated areas and their potential role in regional stress transfer and fault interactions (Daryono, 2016; Massinai et al., 2024; Trismahargyono et al., 2024). Recent works have nonetheless highlighted the seismotectonic significance of the Poso Fault, particularly following the Mw 6.6 Poso earthquake in 2017 and the Mw 7.5 Palu earthquake in 2018, which redistributed Coulomb stress and potentially advanced failure along the fault (Massinai et al., 2024; Sianipar et al., 2021; Trismahargyono et al., 2024; Wang et al., 2019).

On 24 July 2025, a Mw 5.9 earthquake occurred along the Poso Fault at a shallow depth of ~10 km (2.01°S, 120.78°E), followed less than a month later by another shallow event of similar magnitude on 17 August 2025 (Mw 6.0, 1.27°S, 120.75°E) associated with the Tokararu Fault as seen on Fig. 1b (BMKG, 2025). The spatial and temporal proximity of these events raises a critical seismological question: were the August Tokararu earthquake and its aftershocks independent, or were they dynamically influenced by stress changes induced by the July Poso earthquake? Addressing this question is fundamental for understanding fault interactions and cascading seismic hazards in Central Sulawesi.

Coulomb stress transfer (CST) theory provides a quantitative framework for evaluating whether stress changes caused by one earthquake can promote or inhibit rupture on adjacent faults (Ammon et al., 2020). Numerous studies have demonstrated that even small changes in Coulomb stress, on the order of 0.1-1 bar, can significantly alter the likelihood of triggering subsequent earthquakes in nearby fault systems (He et al., 2018; Golshadi et al., 2023; Chen et al., 2024). This mechanism is particularly relevant in the context of earthquake doublets, where two moderate-to-large events occur in close succession on neighboring faults, as observed in other regions such as Türkiye-Syria and British Columbia-Alaska (He et al., 2018; Golshadi et al., 2023; Chen et al., 2024). Applying this framework to the July-August Sulawesi sequence may reveal whether the Poso earthquake contributed to advancing failure on the Tokararu Fault. While prior studies examined stress changes on the Poso Fault induced by larger regional events such as the 2018 Palu earthquake (Massinai et al., 2024; Sianipar et al., 2021; Wang et al., 2019), no analysis has yet addressed the short-term stress interaction between the Poso and Tokararu Faults

In parallel, high-precision earthquake relocation using the HypoDD method is crucial to better delineate fault structures and accurately map aftershock sequences. Previous studies have shown that conventional earthquake catalogs may blur the geometry of fault planes, whereas HypoDD relocation sharpens hypocenter distributions, often revealing fault-parallel and fault-perpendicular clusters indicative of complex fault interactions (Waldhauser and Ellsworth, 2000; Supendi et al., 2019; Purba et al., 2025). Relocating aftershocks from the July-August sequence can help clarify the responsible fault structures and improve our understanding of how stress redistribution shaped subsequent seismicity.

Finally, geodetic techniques such as Differential Interferometric Synthetic Aperture Radar (DInSAR) provide independent constraints on coseismic deformation. Sentinel-1 SAR time-series enable the detection of ground displacement patterns with centimeter-level accuracy, complementing seismic analyses and helping to infer the slip distribution on fault planes (Jin and Fialko, 2021; Fang et al., 2022; Purba et al., 2024, 2025; Pertiwi et al., 2025). Integrating DInSAR deformation fields with relocated seismicity and Coulomb stress modeling offers a powerful multi-disciplinary approach to investigate fault interaction and stress transfer in Central Sulawesi.

This study aims to investigate the relationship between the July Poso and August Tokararu earthquakes through a combined analysis of Coulomb stress transfer, earthquake relocation, and DInSAR deformation mapping. Specifically, we address (1) the evaluation of Coulomb stress changes to assess the potential for stress transfer between the events, (2) the relocation of aftershocks to refine hypocenter distribution and confirm the association of seismicity with the mapped Poso and Tokararu Faults, and (3) the measurement of surface deformation to characterize coseismic displacement.

Although both the Poso and Tokararu Faults have been recognized in previous seismotectonic assessments (e.g., Daryono, 2016; Irsyam et al., 2020; PuSGeN, 2017, 2024), and recent studies have examined the long-term stress adjustments on the Poso Fault following the 2017 and 2018 events (Massinai et al., 2024; Sianipar et al., 2021; Wang et al., 2019), no integrated study has yet investigated their recent seismic interactions. In particular, the July-August 2025 earthquake sequence provides a unique case of spatially and temporally adjacent events, raising the question of whether the Tokararu earthquake was dynamically influenced by the preceding Poso event. By combining Coulomb stress modeling, aftershock relocation, and DInSAR deformation analysis, this study provides a novel contribution to understanding fault interactions in Central Sulawesi. Such an approach has not yet been applied to this fault system, and the findings are expected to enhance regional seismic hazard evaluation.

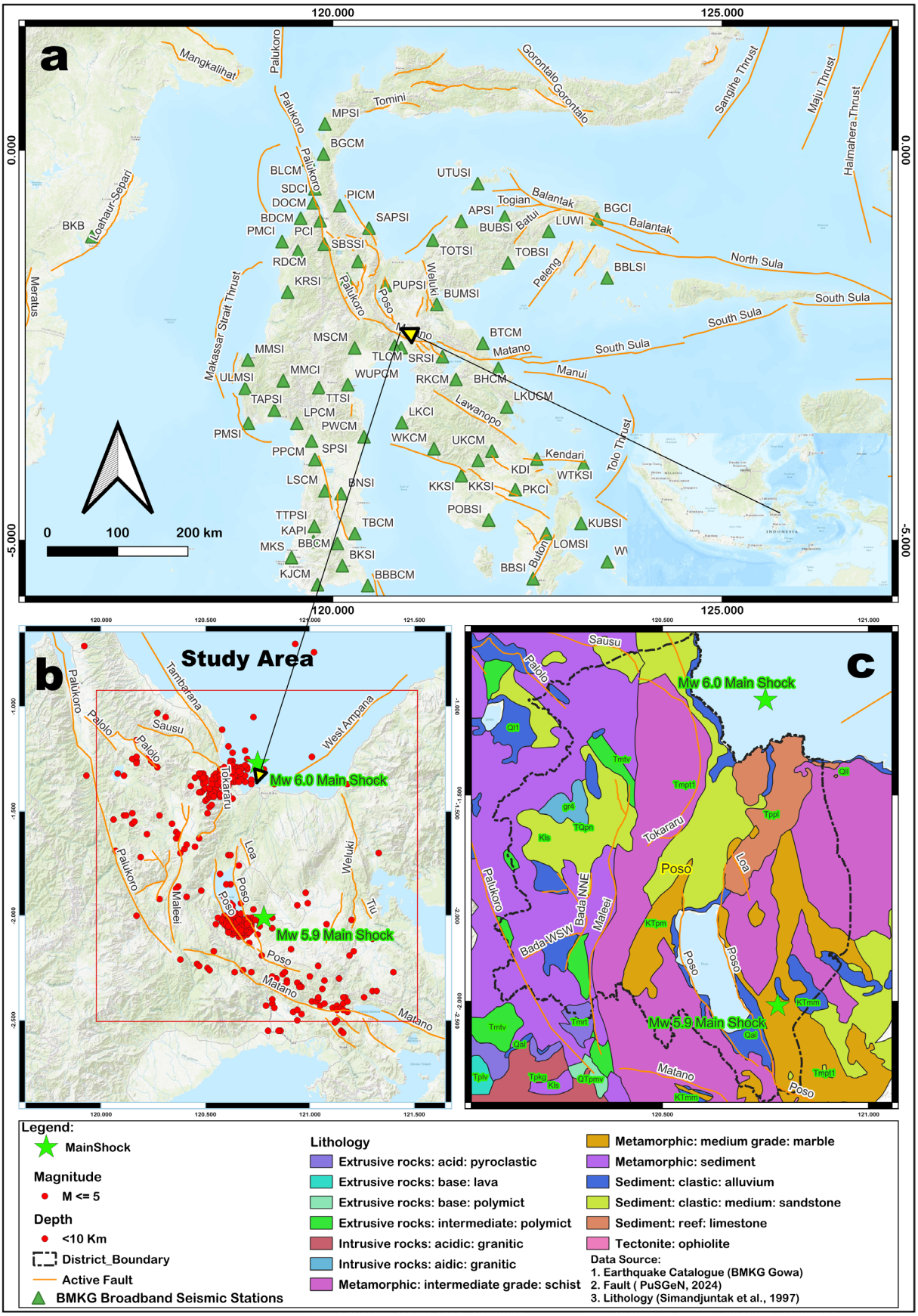

Figure 1. (a) Map of Active Faults and BMKG Broadband Seismic Stations around Sulawesi Island. (b) Earthquake events before relocation in the Poso region and its surroundings. (c) Lithology of the research area.

2. Data and Methods

2.1 Coulomb Stress Change Analysis

To evaluate the interaction between the July 24, 2025 Poso earthquake (Mw 5.9, depth 10 km) and the August 17, 2025 Tokararu earthquake (Mw 6.0, depth 10 km), we investigated the coseismic variation of the Coulomb failure stress(ΔCFS). The Coulomb failure framework is widely used to quantify how slip on a source fault modifies the surrounding stress field and alters the failure tendency of nearby receiver faults (King et al., 1994; Toda et al., 2011).

The change in Coulomb failure stressis expressed as:

$$\Delta CFS = \Delta\tau + \mu'\Delta\sigma_n \quad (1)$$

Where: $\Delta\tau$ is the shear stress change resolved in the slip direction of the receiver fault, $\Delta\sigma_n$ represents the normal stress change acting on the receiver fault plane (positive values indicate fault unclamping), and μ' is the effective friction coefficient that accounts for the influence of pore-fluid pressure. Positive ΔCFS values indicate an increased tendency toward fault failure, whereas negative values indicate stress inhibition or the development of stress shadows.

Coseismic ΔCFS was calculated using Coulomb 3.4 (Toda et al., 2011), which implements elastic dislocation theory for a homogeneous, isotropic half-space. Source fault parameters included fault geometry (strike, dip, and rake), hypocentral location, rupture depth, and earthquake magnitude. Focal mechanism solutions were obtained from the GEOFON Program (GFZ Potsdam) focal mechanism catalog (Saul et al., 2011), indicating a strike-slip mechanism for the Poso earthquake and a thrust mechanism for the Tokararu earthquake. These focal mechanisms were used to define the geometry and slip sense of the source faults in the Coulomb failure modeling.

Receiver faults were explicitly defined according to the mapped geometries of the Poso Fault and Tokararu Fault, based on the PuSGeN geological maps (2017, 2024). An effective friction coefficient of $\mu' = 0.4$ was adopted, consistent with commonly used values for upper-crustal faults (King et al., 1994; Nalbant et al., 2005; Pollitz et al., 2006; Qiu and Chan, 2019; Wang et al., 2014). The resulting ΔCFS maps were analyzed to assess whether stress loading induced by the July 2025 Poso earthquake promoted failure along the Tokararu Fault, potentially contributing to the occurrence of the August 2025 Tokararu earthquake. We used both of relocated main event parameters as input parameters in coulomb stress, which each mainshocks processed using specified receiver fault as shown in Table 1.

Table 1. Coulomb stress change parameter.

Parameter	Poso Fault	Tokararu Fault	References
Longitude	120.722703	120.508250	BMKG (2025)
Latitude	−2.122871	−1.370395	
Depth (km)	10	10	
Magnitude	5.9	6.0	
Strike	306°	191°	Saul et al. (2011)
Dip	84°	54°	
Rake	−15°	104°	
Friction Coefficient	0.4	0.4	King et al., 1994; Nalbant et al., 2005; Pollitz et al., 2006; Qiu and Chan, 2019; Wang et al., 2014

Parameter	Poso Fault	Tokararu Fault	References
Length (km)	11.32	10.31	Wells and Coppersmith (1994)
Width (km)	6.47	6.85	
Max slip (m)	0.35	0.5	Lisle and Walker (2013)

2.2 Relocation of Aftershocks

Precise earthquake locations are essential to delineate active fault structures and to evaluate their relation to mapped surface traces (Purba et al., 2025). In this study, aftershocks associated with the July 24 and August 17, 2025 earthquakes were relocated using the double-difference algorithm implemented in HypoDD program (Waldhauser and Ellsworth, 2000; Waldhauser, 2001). This method minimizes relative travel-time residuals between pairs of nearby earthquakes recorded at common stations, thereby improving relative location accuracy while reducing the influence of velocity model uncertainties.

The input dataset consisted of the regional earthquake catalog provided by the Gowa Geophysical Station, BMKG, spanning July-August 2025. The dataset was obtained from continuous broadband seismic station recordings, illustrated as green triangles in Fig. 1a. In total, 669 seismic events were detected, comprising mainshocks and aftershocks, with magnitudes ranging between 1.1 and 6.0.

Phase arrival times (P- and S-waves) were carefully re-picked where necessary, and only events with a minimum of six high-quality phase readings were retained. Following Waldhauser and Ellsworth (2000), differential times were derived from both catalog picks and waveform cross-correlation for closely spaced event pairs. The relocation was performed using a IASP91 velocity model (Kennett and Engdahl, 1991; Kennett et al., 1995).

The relocation procedure yields high-resolution hypocenter distributions, sharpening the geometry of aftershock clusters. These results allow us to confirm whether seismicity aligns with the Poso and Tokararu Faults mapped by PuSGeN (2017, 2024), and to assess whether the distribution of aftershocks correlates with regions of increased Coulomb stress calculated in Section 2.1.

2.3 DInSAR Deformation Analysis

Ground deformation associated with the 2025 Poso and Tokararu earthquakes was investigated using Differential Interferometric Synthetic Aperture Radar (DInSAR). Sentinel-1 SAR data (Table 1) in ascending track were acquired from the Alaska Satellite Facility (ASF) for dates spanning pre- and post-seismic periods (5 July, 17 July, 29 July, 10 August, 16 August, and 22 August 2025).

Only ascending-track Sentinel-1A data were employed in this study because descending acquisitions exhibited severe coherence loss over the mountainous and densely vegetated areas of Central Sulawesi. InSAR coherence in tropical regions is strongly affected by vegetation density, humidity, and temporal decorrelation associated with seasonal growth cycles (Chindo et al., 2022; Li et al., 2023). Within humid tropical settings, coherence values exceeding 0.6 are typically confined to less than 10 % of the area, while dense forest cover and high soil-moisture variability substantially reduce phase stability (Chindo et al., 2022). In addition to coherence considerations, the selection of ascending orbits was also guided by data coverage and computational constraints. The ascending Sentinel-1 track (path 112, frame 1173) provides full spatial coverage of the Poso-Tokararu region within a single scene, allowing efficient processing and minimizing potential edge artifacts at scene boundaries. In contrast, descending data would require mosaicking two adjacent wide-swath scenes to fully cover the study area, substantially increasing processing time and the risk of geometric distortions across scene overlaps. Similar issues related to multi-frame mosaicking in interferometric processing have been noted in tropical regions where temporal decorrelation is already significant (Ullmann et al., 2019; Chindo et al., 2023). Therefore, the use of ascending-track interferograms was considered the most reliable and computationally efficient configuration for extracting line-of-sight deformation in the

Poso-Tokararu region. These datasets provide coverage of both events and enable the construction of interferograms capturing coseismic displacement.

Although classical DInSAR provides valuable measurements of ground displacement along the radar line-of-sight (LOS), it is inherently less sensitive to motion oriented perpendicular to the LOS, particularly north-south displacement along strike-slip faults. This geometric limitation can cause horizontal movements to be partially projected into apparent uplift-subsidence signals (Ramzan et al., 2022). To address this, complementary techniques such as Pixel Offset Tracking (POT) and Multiple Aperture Interferometry (MAI) have been developed to capture horizontal and along-track deformation components that conventional interferometry may underestimate (Gray et al., 1998; Bechor and Zebker, 2006; Cai et al., 2023; Lin et al., 2024; Xu et al., 2021). POT enables the measurement of large surface offsets by correlating image intensity patterns, while MAI extracts along-track (north-south) displacements from a single interferometric pair. Although these approaches were not applied in this study, they are noted here as promising methods to complement Sentinel-1 DInSAR analyses of strike-slip faults in future work.

The processing workflow followed standard procedures implemented in the ESA SNAP software (ESA, 2012), including precise orbit correction, coregistration, interferogram generation, removal of topographic phase using the SRTM 30 m DEM, filtering, phase unwrapping, and geocoding (Markogiannaki et al., 2020; Purba et al., 2024, 2025; Pertiwi et al., 2025). Interferometric coherence was evaluated to assess phase reliability. In the Poso region, coherence values ranged from 0.06 to 0.88 (5-17 July), 0.11 to 0.90 (17-29 July), and 0.005 to 0.89 (5-29 July), while in the Tokararu region, coherence values ranged from 0.07 to 0.80 (10-16 August), 0.013 to 0.94 (16-22 August), and 0.002 to 0.80 (10-22 August). Areas with coherence above 0.4, predominantly in flat and less vegetated zones, were used for deformation analysis. Lower coherence in forested and hilly terrains reflects strong temporal decorrelation and limited canopy penetration of Sentinel-1's C-band radar (5.4 cm wavelength), consistent with observations in other tropical environments (Chindo et al., 2023; Hatch et al., 2020).

Although L-band systems such as ALOS-2 PALSAR generally maintain higher coherence in vegetated regions due to their longer wavelength (~23 cm), Sentinel-1 C-band data were preferred for this study because of their shorter revisit interval (12 days), wider swath coverage (250 km IW mode), and higher spatial resolution (~20 m), which are crucial for resolving short-term co- and pre-seismic deformation (Wang et al., 2018; Vajedian et al., 2018; Koukouvelas et al., 2021; He et al., 2020). The complete coverage of the Poso-Tokararu fault zone within a single Sentinel-1 frame avoided the need for multi-scene mosaicking, thereby minimizing geometric distortions and boundary artifacts. Moreover, Sentinel-1 data have demonstrated good agreement with ALOS-2 deformation estimates in recent comparative studies (Mehrabi et al., 2019; Peters et al., 2024). Although the C-band is more susceptible to volume scattering from vegetation, the combination of high temporal sampling and coherence filtering ensures that deformation signals were captured reliably in coherent zones.

Only pixels with coherence >0.3 were retained for phase unwrapping and subsequent deformation mapping. Pairs spanning the Poso earthquake (17-29 July) and the Tokararu earthquake (16-22 August) were selected as the primary coseismic interferograms. Pre-seismic (5-17 July, 10-16 August) and longer pre-post pairs (5-29 July, 10-22 August) were also analyzed to provide baseline reference and consistency checks.

Table 2. The Sentinel 1 data.

No.	Acquisition Date	Beam Mode	Polarization	Flight Direction
1	5 July 2025	IW	VV	Ascending
2	17 July 2025	IW	VV	Ascending
3	29 July 2025	IW	VV	Ascending
4	10 August 2025	IW	VV	Ascending
5	16 August 2025	IW	VV	Ascending
6	22 August 2025	IW	VV	Ascending

Line-of-sight (LOS) displacement maps were extracted from the unwrapped interferograms (Chen and Zebker, 2002). Positive values indicate motion toward the satellite, while negative values correspond to motion away from the satellite. To reduce atmospheric and orbital artifacts, multilooking and Goldstein filtering were applied (Goldstein and Werner, 1998). The resulting deformation fields were used to quantify the spatial extent and amplitude of coseismic displacement, and to compare with aftershock distributions and stress transfer models.

3. Results

3.1 Stress Transfer, Aftershock Relocation, and Fault Interaction

The July 24, 2025 Poso earthquake (Mw 6.0) and the August 16, 2025 Tokararu earthquake (Mw 6.0) occurred on distinct faults with contrasting kinematics. Based on the GFZ focal mechanisms, the Poso Fault is characterized by a near-vertical strike-slip motion (strike 306°, dip 84°, rake −15°), whereas the Tokararu Fault displays a thrust mechanism (strike 191°, dip 54°, rake 104°). These contrasting fault types underline their different tectonic roles, with the Poso Fault acting as a lateral shear structure and the Tokararu Fault accommodating compressional uplift.

A total of 669 seismic events were relocated using the HypoDD algorithm, of which 568 were retained (Fig. 2). Prior to relocation, seismic events (green circles) display a relatively diffuse spatial distribution, with considerable

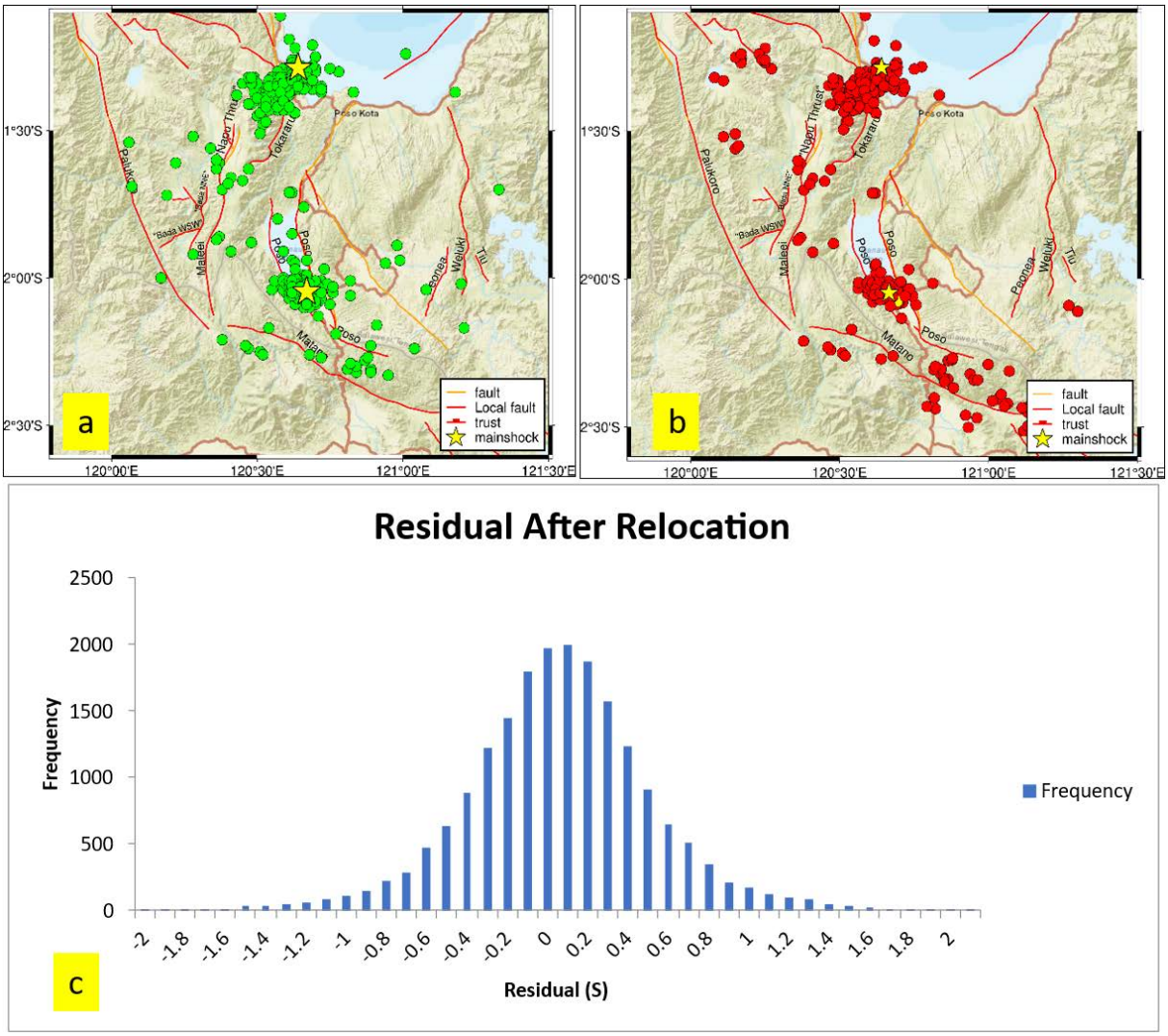

Figure 2. Comparison of results before and after relocation of two series of Poso earthquakes. (a) Map before relocation of all events. (b) Map after relocation. (c) Residual After Relocation.

scatter both laterally and along fault traces. Although the general concentration of seismicity broadly corresponds to the Poso and Tokararu fault systems, the pre-relocation catalog exhibits limited capability to resolve individual fault segments or fault-plane geometries. In particular, hypocenters are widely dispersed across the fault zone, obscuring the distinction between strike-slip and thrust-related deformation.

After relocation (red circles), the seismicity patterns become markedly sharper and more organized. The aftershocks of the Poso mainshock cluster tightly along the Poso-West fault segment, closely following the mapped surface trace of the fault. This improved alignment indicates that the pre-relocation scatter largely reflects location uncertainties rather than true off-fault seismicity. The relocated Poso sequence clearly delineates a linear structure consistent with strike-slip faulting, reinforcing the interpretation that rupture occurred on the mapped Poso Fault rather than on subsidiary or previously unmapped structures. The relocated catalog reveals that aftershocks of the Poso mainshock are concentrated along the Poso-West segment, aligning with the mapped trace of the fault. In contrast, the Tokararu sequence delineates a dipping plane consistent with thrust geometry, with shallow aftershocks (<10 km) outlining the rupture surface. The relocation also shifted the Tokararu mainshock hypocenter southwestward, aligning more closely with the mapped trace of the Tokararu Fault. The relocation procedure significantly improved hypocentral accuracy, as reflected by a substantial reduction in RMS travel-time residuals. Most post-relocation RMS values range between −0.8 and 0.8 s (Fig. 2c), indicating a marked increase in location precision compared to the pre-relocation catalog. This quantitative improvement supports the interpretation that the sharpened seismicity patterns primarily result from enhanced location accuracy rather than changes in seismic source distribution.

The contrast between the diffuse pre-relocation seismicity and the structurally coherent post-relocation patterns underscores the importance of hypocenter relocation for accurately resolving fault geometry, rupture extent, and fault segmentation.

Coulomb stress modeling highlights contrasting stress redistribution patterns associated with the two earthquakes (Fig. 3). The calculations were performed by resolving stress changes onto a single prescribed receiver fault geometry, representative of the dominant fault kinematics in the study area, rather than onto optimally oriented faults. As such, the resulting ΔCFS patterns should be interpreted as scenario-based stress changes under a fixed receiver fault assumption.

Under this framework, the Poso earthquake produced four characteristic lobes of ΔCFS, with values ranging from −0.2 to +0.2 MPa, consistent with the expected stress redistribution of a strike-slip rupture resolved onto the adopted receiver fault geometry. Positive lobes are oriented northwest-southeast, broadly parallel to the Poso Fault, while stress shadows extend in the northeast-southwest direction.

In contrast, the Tokararu earthquake generated a thrust-type Coulomb stress pattern, with positive ΔCFS values exceeding 0.2 MPa concentrated near the rupture tips and extensive negative stress changes forming to the east and west. These patterns reflect the interaction between the source fault geometries and the assumed receiver fault orientation, rather than the full variability expected from an optimally oriented fault approach.

Importantly, within this modeling framework and using the GFZ source parameters, no significant positive ΔCFS is observed on the Tokararu receiver fault following the Poso rupture. This suggests that, under the adopted receiver fault assumption, the two earthquakes were mechanically independent despite their close temporal proximity.

The vertical cross-sections of Coulomb failure stress(ΔCFS) provide additional insight into the depth-dependent stress redistribution associated with the two earthquakes (Fig. 3). Stress changes are resolved onto a single prescribed receiver fault geometry, consistent with the adopted fault kinematics, and should therefore be interpreted within the context of this fixed receiver assumption.

Along cross-section A-A′, the ΔCFS pattern associated with the (Tokararu/Poso) earthquake exhibits a pronounced lobate structure extending from shallow depths to approximately (depth range, e.g., 20-25 km). Positive ΔCFS values dominate near the central portion of the rupture plane and at its downdip termination, indicating zones where the assumed receiver fault is promoted toward failure. In contrast, negative ΔCFS values form adjacent stress-shadow regions, particularly on the flanks of the rupture, reflecting inhibition of failure under the same receiver fault geometry.

The distribution of aftershocks shows a clear spatial association with regions of positive or near-zero ΔCFS, particularly at intermediate depths, whereas fewer events are observed within areas characterized by strongly negative stress changes. This correspondence suggests that, under the adopted receiver fault configuration, the modeled Coulomb stress changes provide a first-order explanation for the observed seismicity distribution.

Cross-section B-B′ reveals a contrasting stress pattern, with positive ΔCFS concentrated at shallower depths beneath the main rupture zone and transitioning into negative stress changes at greater depths. The asymmetric

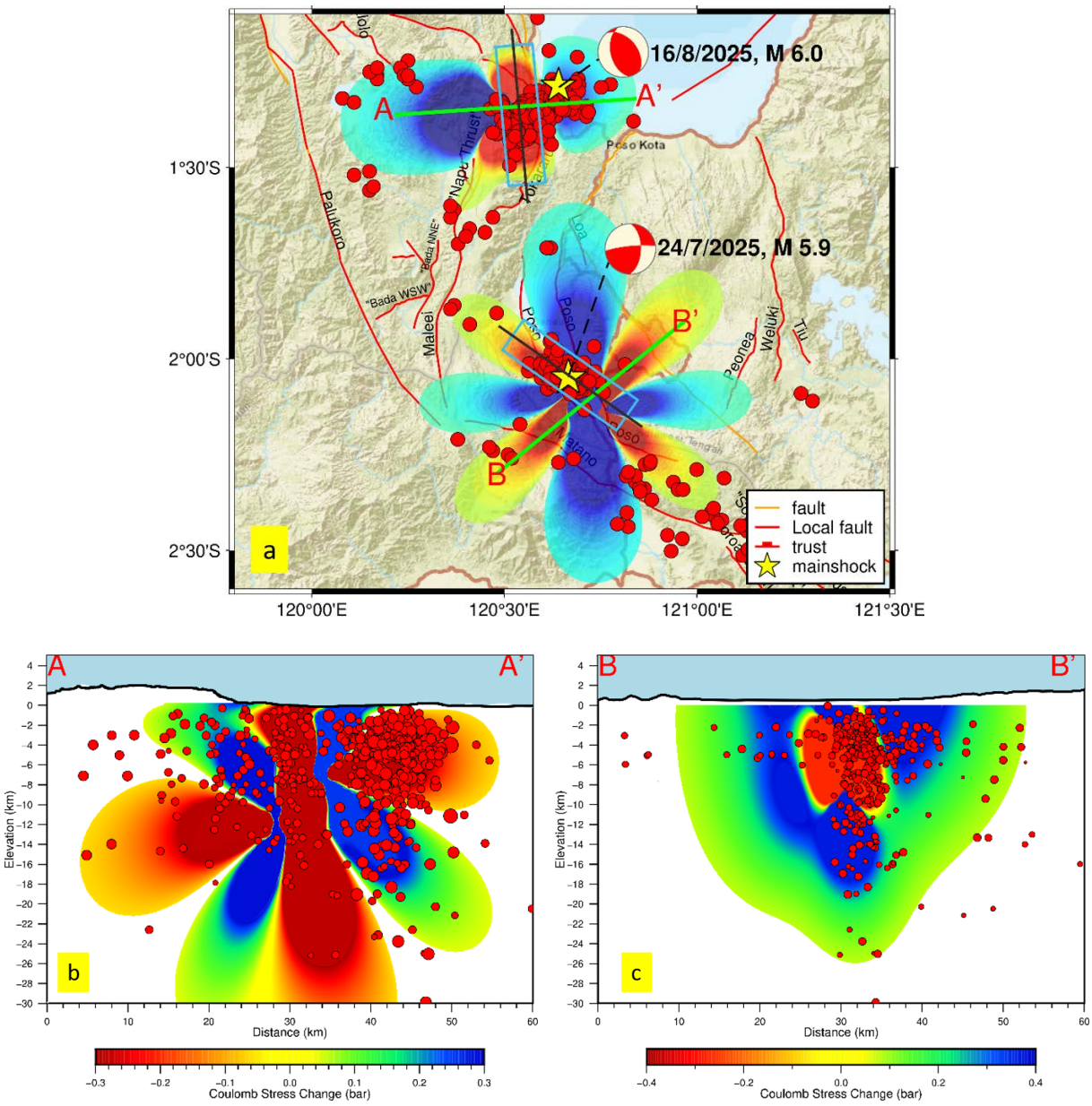

Figure 3. (a) Coulomb stress map of the Poso earthquake and the Tokararu earthquake. (b) Vertical cross section of Tokararu earthquake. (c) Vertical cross section of Poso earthquake.

geometry of the stress lobes reflects the interaction between the rupture geometry and the assumed receiver fault orientation, rather than variations in the regional stress field. Notably, no continuous zone of positive ΔCFS is observed linking the rupture planes of the two earthquakes, indicating an absence of significant stress loading between them in the vertical dimension.

Overall, the vertical cross-section analysis supports the interpretation that the two earthquakes were mechanically independent within the constraints of the single receiver fault Coulomb stress model. While alternative receiver fault orientations or an optimally oriented fault approach could modify the detailed stress distribution, such analyses are beyond the scope of this study.

3.2 Surface Deformation from DInSAR

The ascending-track DInSAR analysis reveals contrasting deformation styles for the July 24, 2025 Poso earthquake (Mw 5.9) and the August 17, 2025 Tokararu earthquake (Mw 6.0).

For the Poso Fault (Fig. 4), the pre-seismic interferogram (5-17 July 2025) shows measurable ground displacement, with uplift reaching +16 cm and subsidence up to −13 cm. This significant deformation prior to rupture suggests the occurrence of precursory processes such as slow slip or aseismic creep along the Poso segment. During the co-seismic period (17-29 July 2025), deformation persisted with uplift of about +13.9 cm and subsidence of −12 cm. The cumulative signal (5-29 July) confirms a similar magnitude (+11.7 cm uplift and −12 cm subsidence), demonstrating spatial overlap between pre-seismic and co-seismic displacements. The deformation field is asymmetric across the fault trace and trends NW-SE, consistent with the nearly vertical left-lateral strike-slip mechanism from the GFZ solution (strike 306°, dip 84°, rake −15). The apparent uplift-subsidence asymmetry primarily reflects the projection of horizontal east-west strike-slip displacement into the satellite line-of-sight (LOS) geometry, rather than purely vertical motion.

In contrast, the Tokararu Fault (Fig. 5) displays a deformation field typical of thrust motion. The pre-seismic interval (10-16 August 2025) shows localized uplift of +12 cm and subsidence of −7.5 cm, indicating strain accumulation prior to the Mw 6.0 rupture. The co-seismic interferogram (16-22 August 2025) records intensification of deformation, with uplift of +11.7 cm and subsidence of −14 cm. The cumulative displacement over 10-22 August reached +13 cm uplift and −14 cm subsidence, consistent with the thrust geometry derived from GFZ parameters (strike 191°, dip 54°, rake 104). The uplifted hanging wall block overthrusting the footwall explains the strong vertical component, in agreement with the relocated aftershocks that define a shallow dipping plane (<10 km depth).

Overall, the DInSAR results capture both pre-seismic and co-seismic deformation in Central Sulawesi. The Poso earthquake is dominated by lateral strike-slip motion projected into the LOS, whereas the Tokararu earthquake reveals vertical uplift-subsidence asymmetry characteristic of thrusting. Importantly, the presence of measurable pre-seismic deformation at both faults suggests that aseismic slip and strain accumulation may have prepared the ruptures in advance of the mainshocks.

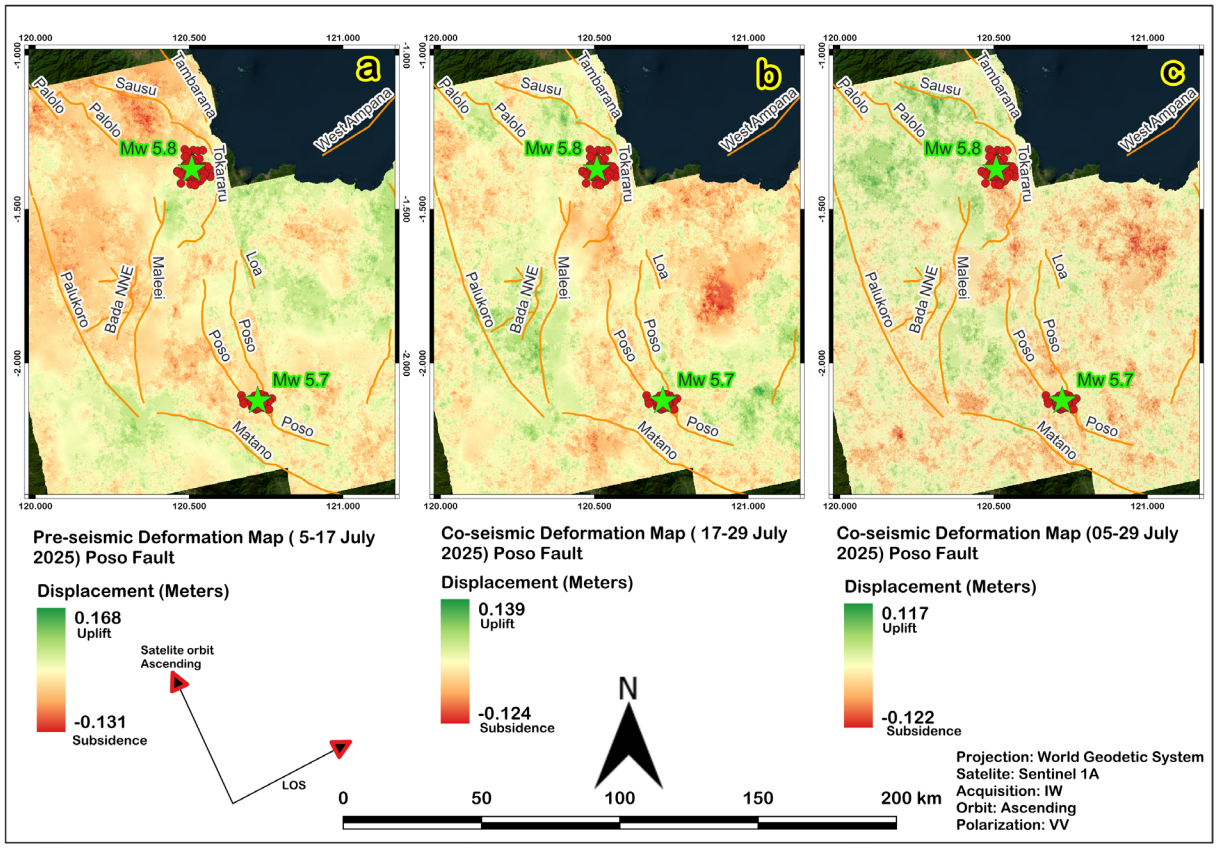

Figure 4. Sentinel-1A ascending-track DInSAR deformation maps for the July 24, 2025 Mw 5.9 Poso earthquake. (a) Pre-seismic deformation (5-17 July), showing LOS displacement up to −13 cm (subsidence) and +16 cm (uplift). (b) Coseismic deformation (17-29 July), with asymmetric displacement of −12 to +13.9 cm across the fault zone. (c) Longer interval (5-29 July) illustrating cumulative deformation and serving as a redundancy check.

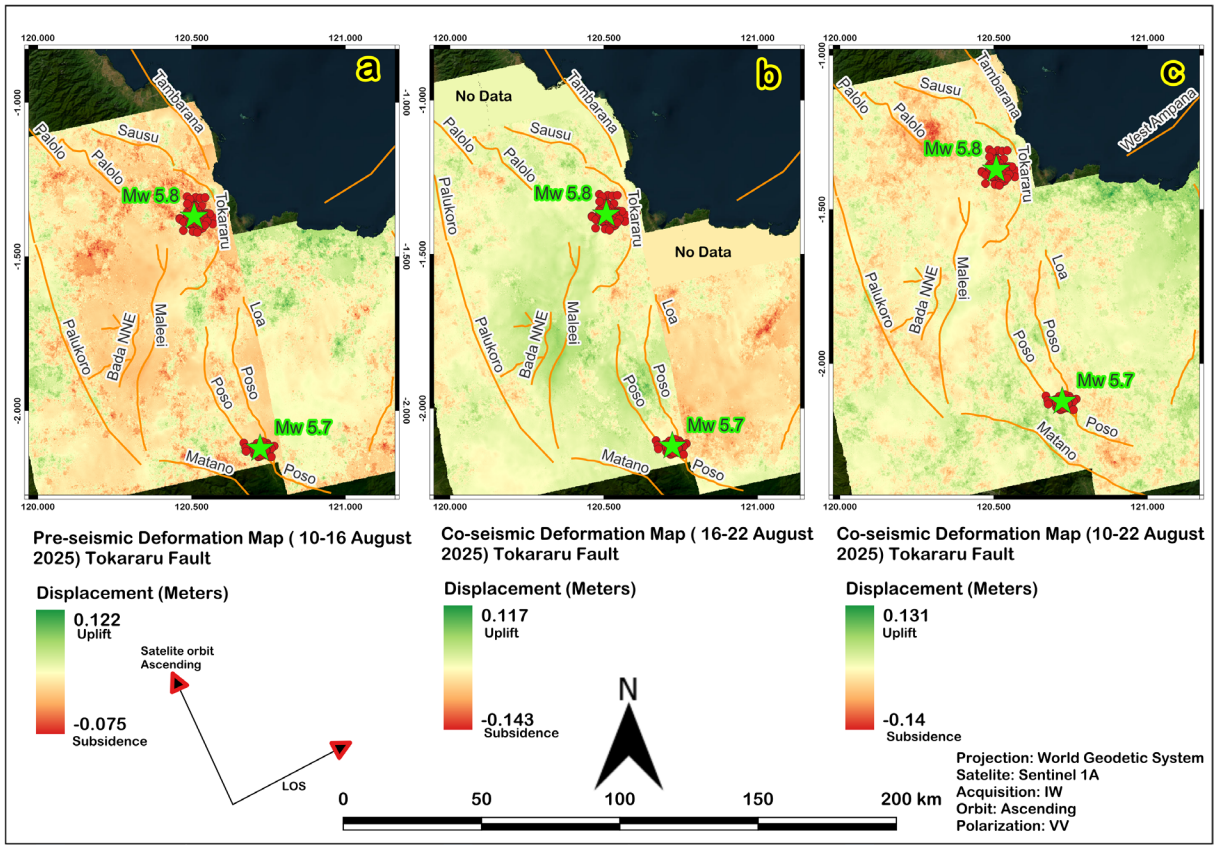

Figure 5. Sentinel-1A ascending-track DInSAR deformation maps for the August 17, 2025 Mw 6.0 Tokararu earthquake. (a) Pre-seismic deformation (10-16 August), showing LOS displacement up to −7.5 cm (subsidence) and +12 cm (uplift). (b) Coseismic deformation (16-22 August), with asymmetric displacement of −14 to +11 cm across the fault zone. (c) Longer interval (10-22 August) illustrating cumulative deformation and serving as a redundancy check.

4. Discussion

The relocated aftershocks provide strong constraints on the geometry of both ruptures (see Fig. 3). In Poso, the clustering of aftershocks near the mainshock and along the Poso-West segment supports activation of the mapped strike-slip fault, consistent with the nearly vertical left-lateral mechanism (strike 306°, dip 84°, rake −15). In Tokararu, the aftershock alignment on a dipping thrust plane with shallow hypocenters confirms a compressional rupture in which the hanging wall was uplifted over the footwall. These contrasting mechanisms emphasize their different tectonic roles: the Poso Fault acting as a lateral shear zone and the Tokararu Fault accommodating vertical shortening. Furthermore, their distinct slip rates (~0.1 mm/yr for Poso versus ~2 mm/yr for Tokararu; PuSGeN, 2017, 2024) highlight their different roles in accommodating intraplate deformation driven by far-field stresses from the convergence of the Australian, Pacific, and Eurasian (Sunda) plates (Hall, 2012; Pasari et al., 2021; Serhalawan and Chen, 2024).

Coulomb stress modeling highlights how stress redistribution controlled aftershock activity. For the Poso earthquake, relocated aftershocks were concentrated near the rupture zone and correlate well with regions of ΔCFS up to +0.2 MPa. Their clustering indicates that static stress transfer played a dominant role in promoting aftershocks, consistent with the sensitivity of faults to stress perturbations as small as 0.01-0.1 MPa (Wu et al., 2016; Liu and Wang, 2014; Ma et al., 2005). In contrast no significant aftershock activity was found within stress shadows. Instead, the distribution follows positive lobes, reinforcing the role of Coulomb stress change in guiding the spatial pattern of seismicity.

For the August 17, 2025 Tokararu earthquake (Mw 6.0), the thrust-fault stress field generated positive lobes (>0.2 MPa) at the northern and southern rupture tips, accompanied by extensive stress shadows on its flanks.

The relocated aftershocks exhibit a near-perfect spatial correlation with these lobes, forming a shallow dipping cluster consistent with the fault geometry. This indicates that the mainshock statically loaded adjacent asperities – locked high-friction fault patches – while surrounding creeping zones accommodated aseismic slip (Toda, 2008). The dense aftershock activity thus effectively maps these asperities that received the greatest static stress increase. When both events are considered together, cumulative Coulomb stress modeling based on GFZ parameters indicates no significant positive transfer from the Poso to the Tokararu Fault. The absence of a stress bridge suggests that Poso and Tokararu ruptured largely independently, though both were embedded within the same regional stress field shaped by far-field convergence (Wu et al., 2016; Liu and Wang, 2014; Ma et al., 2005)..

DInSAR deformation maps provide independent constraints on surface displacements. For the Poso sequence, apparent pre-seismic deformation between 5-17 July shows uplift (+16 cm) and subsidence (−13 cm). However, given the short temporal baseline, low to moderate coherence, and the humid tropical environment, this signal is more likely to reflect a combination of atmospheric artifacts, temporal decorrelation, and phase unwrapping uncertainties, rather than purely tectonic precursory slip. This asymmetric uplift-subsidence pattern is consistent with the nearly vertical strike-slip fault geometry, where horizontal east-west motion is partially projected into the ascending LOS (Qu et al., 2017; Wang and Wright, 2012). Previous studies emphasize that strike-slip ruptures observed in ascending DInSAR tracks can produce apparent uplift-subsidence signals that primarily reflect horizontal slip projected into the LOS (Gourmelen et al., 2011; Milliner et al., 2015; He et al., 2020). However, such geometric projection effects alone do not imply the timing or physical nature of slip, and short-interval pre-seismic interferograms in tropical environments may additionally be influenced by atmospheric delays and decorrelation effects."

The spatial distribution of coherence provides key constraints on the reliability of the observed deformation. In the Poso interferograms, coherent areas with values exceeding 0.6 are primarily located along the fault trace and the basin floor, coinciding with the deformation fringes observed in the interferograms. In contrast, low-coherence zones (<0.3) correspond to heavily vegetated slopes and mountainous terrain where temporal decorrelation, humidity, and atmospheric phase delays can distort phase measurements (Chindo et al., 2023; Mateus et al., 2010). These environmental conditions are typical for tropical regions and can introduce apparent deformation patterns unrelated to true ground motion. However, the fact that coherent zones spatially align with the mapped fault trace suggests that part of the observed pre-seismic signal may reflect genuine ground deformation, possibly related to localized aseismic slip or stress accumulation processes preceding the rupture (Ogata, 2010; Yukutake et al., 2022; Cattania and Segall, 2021; Socquet et al., 2017). Therefore, this deformation is interpreted cautiously as a potential mixture of true deformation and residual atmospheric or processing effects.

The use of Sentinel-1 C-band data, despite the presence of dense tropical vegetation, proved adequate for identifying the main deformation zones when appropriate coherence filtering was applied. Although L-band systems such as ALOS-2 offer improved penetration through vegetation, their longer revisit cycles (14 days) limit temporal resolution and hinder monitoring of rapid deformation transients (Wang et al., 2018; Vajedian et al., 2018). The dense 12-day acquisition interval of Sentinel-1 allowed for the timely detection of both co- and pre-seismic deformation patterns, providing a more continuous temporal record of fault activity. Furthermore, the single-frame coverage of both the Poso and Tokararu epicentral regions minimized geometric inconsistencies, a factor particularly important in rugged topography (He et al., 2020). Consequently, the exclusive use of Sentinel-1 represents a deliberate balance between temporal resolution, spatial coverage, and coherence reliability in a challenging tropical environment (Mehrabi et al., 2019; Peters et al., 2024).

For Tokararu, pre-seismic deformation (10-16 August) reached +12 cm uplift and −7.5 cm subsidence, indicating significant strain accumulation prior to the Mw 6.0 rupture. Co-seismic deformation (16-22 August) shows a similar but stronger pattern (+11.7 to −14 cm), and cumulative analysis (10-22 August) confirms +13 to −14 cm displacement. The deformation field is consistent with thrust kinematics, where the hanging wall was uplifted relative to the footwall, in agreement with aftershock relocation and Coulomb stress modeling. The discrepancy between the short-interval (16-22 August) and the longer-interval (10-22 August) interferograms may reflect the superposition of multiple processes. While the short-interval map captures coseismic deformation, the longer interval also incorporates contributions from pre-seismic strain, coseismic slip, and potentially early post-seismic creep. Similar cumulative effects have been observed in other fault systems, where viscoelastic rebound and aseismic creep significantly influenced deformation fields (Hussain et al., 2016; Thomas et al., 2014; Jolivet et al., 2014). Furthermore, atmospheric artifacts can introduce apparent subsidence signals in longer interferograms, complicating coseismic interpretation (Bekaert et al., 2016; Ma et al., 2021). Previous studies emphasize that the time span of interferograms strongly affects deformation detection, with longer spans often blending pre-, co-, and post-seismic processes (de Michele et al., 2011;

Fattahi and Amelung, 2016). In this context, the enhanced subsidence in the 10-22 August interferogram may not represent purely tectonic signals but rather a mixture of tectonic and atmospheric contributions.

The geological framework of the Pompangeo Complex provides further context for the contrasting rupture behaviors of the Poso and Tokararu earthquakes (Fig. 1c). The Poso Fault cuts through zones of alluvial sediments and weaker cover sequences, which likely facilitated the broad surface deformation captured by InSAR (±12-16 cm uplift and subsidence). Such unconsolidated deposits are mechanically weaker and more prone to aseismic creep, consistent with the observed pre-seismic deformation. In contrast, the Tokararu Fault is rooted in metamorphic basement rocks dominated by schist and marble, which exhibit higher strength and friction. These lithologies tend to host strong asperities that localize rupture nucleation and aftershock activity, as reflected in the tight clustering of relocated aftershocks within positive Coulomb lobes. The mechanical contrast between alluvial and metamorphic domains thus explains the differential surface expressions and rupture styles: Poso acting as a shear-dominated lateral zone with low slip rate (~0.1 mm/yr), and Tokararu as a compressional structure with higher slip rate (~2 mm/yr). Such lithological heterogeneity also governs stress transfer efficiency, where weak sediments may dissipate stress, while strong metamorphic asperities promote localized failure. These findings highlight that the interaction between fault mechanics and the geology of the Pompangeo Complex plays a critical role in shaping rupture dynamics and cascading triggering in Central Sulawesi (Ma et al., 2003; Huang, 2018; Vallage et al., 2016; Hirono et al., 2019; Weng et al., 2016).

Overall, the integration of relocation, Coulomb stress, and DInSAR results provides a coherent picture of the 2025 earthquake. The Poso earthquake initiated local stress redistribution, while the Tokararu earthquake produced strong compressional deformation. Although the Coulomb modeling suggests that the two faults were not directly linked by stress transfer, the InSAR observations, particularly pre-seismic deformation, reveal evidence of aseismic slip and strain accumulation preceding both mainshocks. Together, these findings highlight the complex interactions between tectonic loading, local geology, and fault mechanics in Central Sulawesi, underscoring the potential for moderate earthquakes to redistribute stress across multiple faults and enhance seismic hazard complexity (Segou and Parsons, 2014; Kilb, 2003; Wulur et al., 2025; Xie et al., 2010).

5. Conclusions

This study shows that the 2025 Poso and Tokararu earthquakes, though distinct in kinematics and slip rates, were closely tied to the regional tectonic framework of Central Sulawesi. Aftershock relocation confirmed rupture along the mapped Poso strike-slip and Tokararu thrust faults, while Coulomb stress modeling revealed that aftershocks were concentrated within positive lobes, validating static stress transfer as the dominant control. However, the stress transfer models indicate no significant stress bridge between the two events, suggesting that Poso and Tokararu ruptured largely independently within a shared stress field shaped by far-field plate convergence. DInSAR observations provide independent constraints on deformation, capturing both co-seismic displacement and significant pre-seismic signals that point to aseismic slip and progressive strain accumulation. The geological framework of the Pompangeo Complex, with its juxtaposition of weak alluvium and strong metamorphic rocks, influenced rupture localization, deformation style, and aftershock clustering. These findings emphasize that moderate inland earthquakes in Sulawesi can generate complex, multi-fault responses shaped by both mechanical and geological factors. Future research should incorporate local 3D velocity models to improve relocation, heterogeneous elastic structures in Coulomb modeling, and complementary descending-track DInSAR to resolve full 3D deformation. Such refinements will enhance seismic hazard assessment in this tectonically complex region.

Data availability statement. The relocated earthquake catalog used in this study can be accessed upon reasonable request from the Gowa Geophysical Station, Agency for Meteorology, Climatology, and Geophysics (BMKG). Sentinel-1 SAR data are publicly available through the Alaska Satellite Facility (ASF) at https://search.asf.alaska.edu/.

Acknowledgements. The authors gratefully acknowledge the Meteorology, Climatology, and Geophysics Agency (BMKG), particularly the Gowa Geophysical Station team, for their support in completing this research. We also extend our sincere appreciation to the two anonymous reviewers for their insightful comments and constructive suggestions, which significantly enhanced the quality of this manuscript.

References

Ammon, C. J., A. A. Velasco, T. Lay and T. C. Wallace (2020). Foundations of Modern Global Seismology, in Foundations of Modern Global Seismology, doi:10.1016/B978-0-12-815679-7.00002-1.

Bechor, N. and H. A. Zebker (2006). Measuring two-dimensional movements using a single InSAR pair, Geophys. Res. Lett., 33, 16, L16311, doi:10.1029/2006GL026883.

Bekaert, D., P. Segall, T. Wright and A. Hooper (2016). A network inversion filter combining GNSS and InSAR for tectonic slip modeling, J. Geophys. Res. Solid Earth, 121, 3, 2069-2086, doi:10.1002/2015JB012638.

BMKG (2025). Ulasan guncangan tanah akibat gempabumi barat laut Poso, Sulawesi Tengah, Review of ground shaking due to the northwest Poso earthquake, Central Sulawesi- in Indonesian, Badan Meteorologi, Klimatologi, dan Geofisika, https://www.bmkg.go.id/gempabumi/ulasan-guncangan-tanah/ulasan-guncangan-tanah-akibat-gempabumi-barat-laut-poso-17-agustus-2025.

Cai, J., C. Wang and L. Zhang (2023). Analysis of mass wasting processes in the Slumgullion landslide using multi-track time-series UAVSAR images, Remote Sens., 15, 19, 4746, doi:10.3390/rs15194746.

Cattania, C. and P. Segall (2021). Precursory slow slip and foreshocks on rough faults, J. Geophys. Res. Solid Earth, 126, 4, e2020JB020430, doi:10.1029/2020JB020430.

Cattania, C., S. Hainzl, L. Wang, F. Roth et al. (2014). Propagation of Coulomb stress uncertainties in physics-based aftershock models, J. Geophys. Res. Solid Earth, 119, 10, 7847-7864, doi:10.1002/2014JB011183.

Chen, C. W. and H. A. Zebker (2002). Phase unwrapping for large SAR interferograms: Statistical segmentation and generalized network models, IEEE Trans. Geosci. Remote Sens., 40, 8, 1709-1719, doi:10.1109/TGRS.2002.802453.

Chen, J., C. Liu, L. Dal Zilio, J. Cao et al. (2024). Decoding stress patterns of the 2023 Türkiye-Syria earthquake doublet, J. Geophys. Res. Solid Earth, 129, 10, e2024JB029213, doi:10.1029/2024JB029213.

Chindo, M. M., M. Hashim and A. W. Rasib (2022). Interferometric synthetic aperture radar coherence constraints in heavily vegetated tropics, IOP Conf. Ser., Earth Environ. Sci., 1064, 1, 012027, doi:10.1088/1755-1315/1064/1/012027.

Daryono, M. R. (2016). Paleoseismologi Tropis Indonesia Dengan Studi Kasus di Sesar Sumatra, Sesar Palukoro-Matano, dan Sesar Lembang, Paleoseismology of Tropical Indonesia Cases study in Sumatran Fault, Palukoro-Matano Fault, and Lembang Fault, in Indonesian, with an English Abstract, Doctoral Dissertation, in Earth Science Doctoral Programme, Bandung Institute of Technology, 208.

de Michele, M., D. Raucoules, F. Rolandone, P. Briole et al. (2011). Spatiotemporal evolution of surface creep in the Parkfield region of the San Andreas fault (1993-2004) from synthetic aperture radar, Earth Planet. Sci. Lett., 308, 1-2, 141-150, doi:10.1016/j.epsl.2011.05.049.

ESA (2012). Sentinel-1: ESA's radar observatory mission for GMES operational services, ESA Spec. Publ., 1322.

Fang, J., Q. Ou, T. J. Wright, R. Okuwaki et al. (2022). Earthquake cycle deformation associated with the 2021 Mw 7.4 Maduo earthquake: An intrablock rupture event on a slow-slipping fault from Sentinel-1 InSAR and teleseismic data, J. Geophys. Res. Solid Earth, 127, 11, e2022JB024268, doi:10.1029/2022JB024268.

Fattahi, H. and F. Amelung (2016). InSAR observations of strain accumulation and fault creep along the Chaman fault system, Pakistan and Afghanistan, Geophys. Res. Lett., 43, 16, 8399-8406, doi:10.1002/2016GL070121.

Frando, M., P. Ariyanto, J. Purba and T. M. Apriliaji (2025). Gravity-anomaly-based analysis of surface ruptures along the Palu-Koro fault (Indonesia) for long-term seismic hazard mitigation, Bull. Geogr. Phys. Geogr. Ser., 28, 81-101, doi:10.12775/bgeo-2025-0006.

Goldstein, R. M. and C. L. Werner (1998). Radar interferogram filtering for geophysical applications, Geophys. Res. Lett., 25, 21, 4035-4038, doi:10.1029/1998GL900033.

Golshadi, Z., N. A. Famiglietti, R. Caputo, S. SoltaniMoghadam et al. (2023). Contemporaneous thick- and thin-skinned seismotectonics in the external Zagros: The case of the 2021 Fin doublet, Iran, Remote Sens., 15, 12, 2981, doi:10.3390/rs15122981.

Gray, A. L., K. E. Mattar, P. W. Vachon, R. Bindschadler et al. (1998). InSAR results from the RADARSAT Antarctic mapping mission data: Estimation of glacier motion using a simple registration procedure, IGARSS Proc., 3, 1203-1205, doi:10.1109/IGARSS.1998.691662.

Hainzl, S., B. Enescu, M. Cocco, J. Woessner et al. (2009). Aftershock modeling based on uncertain stress calculations, J. Geophys. Res. Solid Earth, 114, 5, B05309, doi:10.1029/2008JB006011.

Hall, R. (2012). Late Jurassic-Cenozoic reconstructions of the Indonesian region and the Indian Ocean, Tectonophysics, 570-571, 1-41, doi:10.1016/j.tecto.2012.04.021.

Hanif, M., L. Handayani, A. R. Puji, A. Patria et al. (2024). Gravity modelling insights into crustal structure: Moho depth and subsurface structures in Central Sulawesi, IOP Conf. Ser.: Earth Environ. Sci., 1373, 1, 012050, doi:10.1088/1755-1315/1373/1/012050.

Hardebeck, J. L. (2014). The impact of static stress change, dynamic stress change, and the background stress on aftershock focal mechanisms, J. Geophys. Res. Solid Earth, 119, 11, 8364-8380, doi:10.1002/2014JB011533.

Hatch, R. L., R. E. Abercrombie, C. J. Ruhl and K. D. Smith (2020). Evidence of aseismic and fluid-driven processes in a small complex seismic swarm near Virginia City, Nevada, Geophys. Res. Lett., 47, 4, e2019GL085477, doi:10.1029/2019GL085477.

He, X., S. Ni, P. Zhang and J. T. Freymueller (2018). The 1 May 2017 British Columbia-Alaska earthquake doublet and implications for complexity near the southern end of the Denali fault system, Geophys. Res. Lett., 45, 12, 5937-5947, doi:10.1029/2018GL078014.

He, Z., T. Chen, M. Wang and Y. Li (2020). Multi-segment rupture model of the 2016 Kumamoto earthquake revealed by InSAR and GPS data, Remote Sens., 12, 22, 3721, doi:10.3390/rs12223721.

Hirono, T., K. Tsuda and S. Kaneki (2019). Role of weak materials in earthquake rupture dynamics, Sci. Rep., 9, 1, 11046, doi:10.1038/s41598-019-43118-5.

Huang, Y. (2018). Earthquake rupture in fault zones with along-strike material heterogeneity, J. Geophys. Res. Solid Earth, 123, 11, 9884-9898, doi:10.1029/2018JB016354.

Hussain, E., T. Wright, R. J. Walters, D. Bekaert et al. (2016). Geodetic observations of postseismic creep in the decade after the 1999 Izmit earthquake, Turkey: Implications for a shallow slip deficit, J. Geophys. Res. Solid Earth, 121, 4, 2980-3001, doi:10.1002/2015JB012737.

Irsyam, M., P. R. Cummins, M. Asrurifak, L. Faizal et al. (2020). Development of the 2017 national seismic hazard maps of Indonesia, Earthq. Spectra, 36, 1 suppl., doi:10.1177/8755293020951206.

Jin, Z. and Y. Fialko (2021). Coseismic and early postseismic deformation due to the 2021 Mw 7.4 Maduo (China) earthquake, Geophys. Res. Lett., 48, 21, doi:10.1029/2021GL095213.

Jolivet, R., T. Candela, C. Lasserre, F. Renard et al. (2014). The burst-like behavior of aseismic slip on a rough fault: The creeping section of the Haiyuan fault, China, Bull. Seismol. Soc. Am., 105, 1, 480-488, doi:10.1785/0120140237.

Kennett, B. L. N. and E. R. Engdahl (1991). Traveltimes for global earthquake location and phase identification, Geophys. J. Int., 105, 2, doi:10.1111/j.1365-246X.1991.tb06724.x.

Kennett, B. L. N., E. R. Engdahl and R. Buland (1995). Constraints on seismic velocities in the Earth from traveltimes, Geophys. J. Int., 122, 1, doi:10.1111/j.1365-246X.1995.tb03540.x.

Kilb, D. (2003). A strong correlation between induced peak dynamic Coulomb stress change from the 1992 Mw 7.3 Landers, California, earthquake and the hypocenter of the 1999 Mw 7.1 Hector Mine, California, earthquake, J. Geophys. Res. Solid Earth, 108, 1, doi:10.1029/2001JB000678.

King, G. C. P., R. S. Stein and J. Lin (1994). Static stress changes and the triggering of earthquakes, Bull. Seismol. Soc. Am., 84, 3, doi:10.1016/0148-9062(95)94484-2.

Koukouvelas, I., K. G. Nikolakopoulos, A. Kyriou, R. Caputo et al. (2021). The March 2021 Damasi earthquake sequence, central Greece: Reactivation evidence across the westward propagating Tyrnavos Graben, Geosciences, 11, 8, 328, doi:10.3390/geosciences11080328.

Li, Z., K. Dai, J. Deng, C. Liu et al. (2023). Identifying potential landslides in steep mountainous areas based on improved seasonal interferometry stacking-InSAR, Remote Sens., 15, 13, 3278, doi:10.3390/rs15133278.

Lin, L., R. Y. Chuang, C. Lu, K. Ching et al. (2024). Derivation of 3D coseismic displacement field from integrated azimuth and LOS displacements for the 2018 Hualien earthquake, Remote Sens., 16, 7, 1159, doi:10.3390/rs16071159.

Lisle, R. J. and R. J. Walker (2013). The estimation of fault slip from map data: The separation-pitch diagram, Tectonophysics, 583, doi:10.1016/j.tecto.2012.10.034.

Liu, F. B. and A. G. Wang (2014). Study on aftershocks triggering by static stress changes of the Minxian-Zhangxian 6.6 earthquake, Appl. Mech. Mater., 527, 77-80, doi:10.4028/www.scientific.net/AMM.527.77.

Ma, K., E. E. Brodsky, J. Mori, C. Ji et al. (2003). Evidence for fault lubrication during the 1999 Chi-Chi, Taiwan, earthquake (Mw 7.6), Geophys. Res. Lett., 30, 5, doi:10.1029/2002GL015380.

Ma, K., C. Chan and R. S. Stein (2005). Response of seismicity to Coulomb stress triggers and shadows of the 1999 Mw 7.6 Chi-Chi, Taiwan, earthquake, J. Geophys. Res. Solid Earth, 110, 5, doi:10.1029/2004JB003389.

Ma, Z., J. Liu, X. Liu, C. Zhou et al. (2021). Go extra miles: An additional error correction procedure aimed to further improve phase unwrapping accuracy and reduce creep model uncertainty, J. Geophys. Res. Solid Earth, 127, 1, doi:10.1029/2021JB022478.

Markogiannaki, O., A. Karavias, D. Bafi, D. Angelou et al. (2020). A geospatial intelligence application to support post-disaster inspections based on local exposure information and on co-seismic DInSAR results: The case of the Durres (Albania) earthquake on November 26, 2019, Nat. Hazards, 103, 3, doi:10.1007/s11069-020-04120-7.

Massinai, M. A., M. T. Rafie, T. Razin, M. A. H. Assagaf et al. (2024). Analysis of stress changes on the Poso fault caused by large inland earthquakes: Case study of the 2017 Mw 6.6 Poso and the 2018 Mw 7.5 Palu-Donggala earthquakes, Ann. Geophys., 67, 5, doi:10.4401/ag-9106.

Mateus, P., G. Nico and J. Catalão (2010). Mapping temporal evolution of water vapour in troposphere by interferometric SAR data, Proc. SPIE, doi:10.1117/12.864727.

Mehrabi, H., B. Voosoghi, M. Motagh and R. F. Hanssen (2019). Three-dimensional displacement fields from InSAR through Tikhonov regularization and least-squares variance component estimation, J. Surv. Eng., 145, 4, doi:10.1061/(ASCE)SU.1943-5428.0000289.

Nalbant, S. S., S. Steacy, K. Sieh, D. Natawidjaja et al. (2005). Earthquake risk on the Sunda trench, Nature, 435, 7043, doi:10.1038/nature435756a.

Natawidjaja, D. H., M. R. Daryono, G. Prasetya, U. Udrekh et al. (2021). The 2018 Mw 7.5 Palu supershear earthquake ruptures geological fault multisegments separated by large bends: Results from integrating field measurements, LiDAR, swath bathymetry and seismic-reflection data, Geophys. J. Int., 224, 2, doi:10.1093/gji/ggaa498.

Ogata, Y. (2010). Anomalies of seismic activity and transient crustal deformations preceding the 2005 Mw 7.0 earthquake west of Fukuoka, Pure Appl. Geophys., 167, 8-9, 1115-1127, doi:10.1007/s00024-010-0096-y.

Pasari, S., A. V. H. Simanjuntak, N. Neha and Y. Sharma (2021). Nowcasting earthquakes in Sulawesi Island, Indonesia, Geosci. Lett., 8, 1, doi:10.1186/s40562-021-00197-5.

Pertiwi, I. I., T. Trismahargyono, M. Marniati and J. Purba (2025). Post-seismic surface deformation of the Tarakan earthquake in 2015 using the DInSAR technique, Geoplanning, 12, 1, 79-94, doi:10.14710/geoplanning.12.1.79-94.

Peters, S., J. Liu, G. Keppel, A. Wendleder et al. (2024). Detecting coseismic landslides in GEE using machine learning algorithms on combined optical and radar imagery, Remote Sens., 16, 10, 1722, doi:10.3390/rs16101722.

Pollitz, F. F., P. Banerjee, R. Bürgmann, M. Hashimoto et al. (2006). Stress changes along the Sunda trench following the 26 December 2004 Sumatra-Andaman and 28 March 2005 Nias earthquakes, Geophys. Res. Lett., 33, 6, doi:10.1029/2005GL024558.

Purba, J., Harisma, R. Priadi, R. Amelia et al. (2024). Surface deformation and its implications for land degradation after the 2021 Flores earthquake (Mw 7.4) using differential interferometry synthetic aperture radar, J. Degrad. Min. Lands Manag., 12, 1, 6819-6831, doi:10.15243/jdmlm.2024.121.6819.

Purba, J., R. Priadi, M. Frando and I. Pertiwi (2025). The Purpri fault: A newly identified active fault in East Kolaka, Indonesia, based on HypoDD and DInSAR, Geol. An. Balk. Poluostrva, 86, 1, 121-143, doi:10.2298/gabp250417005p.

PuSGeN. (2017). Peta Sumber dan Bahaya Gempa Indonesia Tahun 2017, Map of Indonesia Earthquake Sources and Hazards in 2017, in Indonesian, PUPR Press, 76.

PuSGeN. (2024). Peta Sumber dan Bahaya Gempa Indonesia Tahun 2024, Map of Indonesia Earthquake Sources and Hazards in 2024, in Indonesian, PUPR Press, 515.

Qiu, Q. and C. H. Chan (2019). Coulomb stress perturbation after great earthquakes in the Sumatran subduction zone: Potential impacts in the surrounding region, J. Asian Earth Sci., 180, 103869, doi:10.1016/j.jseaes.2019.103869.

Ramzan, U., H. Fan, H. Aeman, M. Ali et al. (2022). Combined analysis of PS-InSAR and hypsometry integral for comparing seismic vulnerability and assessment of various regions of Pakistan, Sci. Rep., 12, 1, doi:10.1038/s41598-022-26159-1.

Saul, J., J. Becker and W. Hanka (2011). Global moment tensor computation at GFZ Potsdam, AGU Fall Meet, San Francisco.

Segou, M. and T. Parsons (2014). The stress shadow problem in physics-based aftershock forecasting: Does incorporation of secondary stress changes help?, Geophys. Res. Lett., 41, 11, 3810-3817, doi:10.1002/2013GL058744.

Serhalawan, Y. and P. F. Chen (2024). Seismotectonics of Sulawesi, Indonesia, Tectonophysics, 883, 230366, doi:10.1016/j.tecto.2024.230366.

Sianipar, D., G. Daniarsyad, P. Priyobudi, N. Heryandoko et al. (2021). Rupture behavior of the 2017 Mw 6.6 Poso earthquake in Sulawesi, Indonesia, Geod. Geodyn., 12, 5, 329-335, doi:10.1016/j.geog.2021.07.002.

Simandjuntak, T. O., J. B. Supandjono, S. Surono and T. O. Simandjuntak (1997). Peta geologi lembar Poso, Sulawesi: Geological map of the Poso quadrangle, Sulawesi, Pusat Penelitian dan Pengembangan Geologi.

Socquet, A., J. P. Valdes, J. Jara, F. Cotton et al. (2017). An 8-month slow slip event triggers progressive nucleation of the 2014 Chile megathrust, Geophys. Res. Lett., 44, 9, doi:10.1002/2017GL073023.

Supendi, P., A. D. Nugraha, S. Widiyantoro, C. I. Abdullah et al. (2019). Hypocenter relocation of the aftershocks of the Mw 7.5 Palu earthquake (September 28, 2018) and swarm earthquakes of Mamasa, Sulawesi, Indonesia, using the BMKG network data, Geosci. Lett., 6, 1, doi:10.1186/s40562-019-0148-9.

Thomas, M. Y., J. Avouac, J. Champenois, J. Lee et al. (2014). Spatiotemporal evolution of seismic and aseismic slip on the Longitudinal Valley fault, Taiwan, J. Geophys. Res. Solid Earth, 119, 6, 5114-5139, doi:10.1002/2013JB010603.

Toda, S. (2008). Coulomb stresses imparted by the 25 March 2007 Mw 6.6 Noto-Hanto, Japan, earthquake explain its butterfly distribution of aftershocks and suggest a heightened seismic hazard, Earth Planets Space, 60, 10, 1041-1046, doi:10.1186/BF03352866.

Toda, S., J. Lin and R. S. Stein (2011). Using the 2011 Mw 9.0 off the Pacific coast of Tohoku earthquake to test the Coulomb stress triggering hypothesis and to calculate faults brought closer to failure, Earth Planets Space, 63, 7, 725-730, doi:10.5047/eps.2011.05.010.

Trismahargyono, A., A. Puspita, I. I. Pertiwi, A. Agustan et al. (2024). Surface deformation analysis due to the Poso earthquake on May 29, 2017 using the DInSAR method, IOP Conf. Ser., Earth Environ. Sci., 1373, 1, 012049, doi:10.1088/1755-1315/1373/1/012049.

Ullmann, T., J. A. Sauerbrey, D. Hoffmeister, S. M. May et al. (2019). Assessing spatiotemporal variations of Sentinel-1 InSAR coherence at different time scales over the Atacama Desert (Chile) between 2015 and 2018, Remote Sens., 11, 24, 2960, doi:10.3390/rs11242960.

Vajedian, S., M. Motagh, Z. Mousavi, K. Motaghi et al. (2018). Coseismic deformation field of the Mw 7.3 12 November 2017 Sarpol-e Zahab (Iran) earthquake: A decoupling horizon in the northern Zagros Mountains inferred from InSAR observations, Remote Sens., 10, 10, 1589, doi:10.3390/rs10101589.

Vallage, A., Y. Klinger, R. Lacassin, A. Delorme et al. (2016). Geological structures control on earthquake ruptures: The Mw 7.7 2013 Balochistan earthquake, Pakistan, Geophys. Res. Lett., 43, 19, doi:10.1002/2016GL070418.

Waldhauser, F. (2001). hypoDD: A computer program to compute double-difference hypocenter locations, U. S. Geol. Surv. Open File Rep., 1-113.

Waldhauser, F. and W. L. Ellsworth (2000). A double-difference earthquake location algorithm: Method and application to the northern Hayward fault, California, Bull. Seismol. Soc. Am., 90, 6, doi:10.1785/0120000006.

Wang, J., C. Xu, J. T. Freymueller, Z. Li et al. (2014). Sensitivity of Coulomb stress change to the parameters of the Coulomb failure model: A case study using the 2008 Mw 7.9 Wenchuan earthquake, J. Geophys. Res. Solid Earth, 119, 4, doi:10.1002/2012JB009860.

Wang, S., C. Xu, W. Xu, Z. Yin et al. (2019). The 2017 Mw 6.6 Poso earthquake: Implications for extrusion tectonics in Central Sulawesi, Seismol. Res. Lett., 90, 2A, doi:10.1785/0220180211.

Wang, Z., R. Zhang, X. Wang and G. Liu (2018). Retrieving three-dimensional coseismic deformation of the 2017 Mw 7.3 Iraq earthquake by multi-sensor SAR images, Remote Sens., 10, 6, 857, doi:10.3390/rs10060857.

Wells, D. L. and K. J. Coppersmith (1994). New empirical relationships among magnitude, rupture length, rupture width, rupture area, and surface displacement, Bull. Seismol. Soc. Am., 84, 4, doi:10.1785/BSSA0840040974.

Weng, H., H. Yang, Z. Zhang and X. Chen (2016). Earthquake rupture extents and coseismic slips promoted by damaged fault zones, J. Geophys. Res. Solid Earth, 121, 6, 4446-4457, doi:10.1002/2015JB012713.

Wu, J., Q. Hu, W. Li and D. Lei (2016). Study on Coulomb stress triggering of the April 2015 Mw 7.8 Nepal earthquake sequence, Int. J. Geophys., 2016, 7378920, doi:10.1155/2016/7378920.

Wulur, K. H. C., S. Junaedi, A. Susanto, J. Purba et al. (2025). Hypocenter relocation to identify hidden faults and their environmental implications in the karst region of Maros-Pangkep, South Sulawesi, J. Degrad. Min. Lands Manag., 12, 5, 8663-8676, doi:10.15243/jdmlm.2025.125.8663.

Xie, C., Y. Zhu, X. Lei, Y. Hai-Ying et al. (2010). Pattern of stress change and its effect on seismicity rate caused by the Ms 8.0 Wenchuan earthquake, Sci. China Earth Sci., 53, 9, 1260-1270, doi:10.1007/s11430-010-4025-9.

Xu, L., Q. Chen, J. Zhao, X. Liu et al. (2021). An integrated approach for mapping three-dimensional coseismic displacement fields from Sentinel-1 TOPS data based on DInSAR, POT, MAI and BOI techniques: Application to the 2021 Mw 7.4 Maduo earthquake, Remote Sens., 13, 23, 4847, doi:10.3390/rs13234847.

Yukutake, Y., K. Yoshida and R. Honda (2022). Interaction between aseismic slip and fluid invasion in earthquake swarms revealed by dense geodetic and seismic observations, J. Geophys. Res. Solid Earth, 127, 4, doi:10.1029/2021JB022933.

Appendix.

The six SLC data used in this research are:

a) S1C_IW_SLC__1SDV_20250705T101747_20250705T101814_003083_006434_0644
b) 1C_IW_SLC__1SDV_20250717T101748_20250717T101815_003258_006947_3FEA
c) S1C_IW_SLC__1SDV_20250729T101749_20250729T101816_003433_006E6E_A52B
d) S1C_IW_SLC__1SDV_20250810T101750_20250810T101817_003608_00739C_79CF
e) S1A_IW_SLC__1SDV_20250816T101856_20250816T101928_060559_07882A_1002
f) S1C_IW_SLC__1SDV_20250822T101750_20250822T101817_003783_0078DD_7F35

***CORRESPONDING AUTHOR: Joshua PURBA**,
Gowa Geophysical Station, Agency for Meteorology Climatology and Geophysics, BMKG, Gowa, Indonesia
e-mail: joshua.purba@bmkg.go.id